On the poro-elastic models for microvascular blood flow resistance: an in-vitro validation

Alberto Coccarelli[1] Supratim Saha[2] Tanjeri Purushotham[2]
K. Arul Prakash[2] Perumal Nithiarasu[1,3*]

[1] Biomedical Engineering Group, Zienkiewicz Centre for Computational Engineering, College of Engineering, Swansea University, UK
[2]Department of Applied Mechanics, Indian Institute of Technology Madras, India
[3]VAJRA Adjunct Professor, Indian Institute of Technology Madras, India

Word count: 3474

*Correspondance to p.nithiarasu@swansea.ac.uk

Abstract

Nowadays, adequate and accurate representation of the microvascular flow resistance constitutes one of the major challenges in computational haemodynamic studies. In this work, a theoretical, porous media framework, ultimately designed for representing downstream resistance, is presented and compared against an *in vitro* experimental results. The resistor consists of a poro-elastic tube, with either a constant or variable porosity profile in space. The underlying physics, characterizing the fluid flow through the porous media, is analysed by considering flow variables at different net-work locations. Backward reflections, originated in the reservoir of the *in vitro* model, are accounted for through a reflection coefficient imposed as an outflow network condition. The simulation results are in good agreement with the measurements for both the homogenous and heterogeneous poros-ity conditions. In addition, the comparison allows identification of the range of values representing experimental reservoir reflection coefficients. The pressure drops across the heterogeneous porous media increases with respect to the simpler configuration, whilst flow remains almost unchanged. The effect of some fluid network features, such as tube Young's modulus and fluid viscosity, on the theoretical results is also elucidated, providing a reference for the *in vitro* and *in silico* simulation of different microvascular conditions.

Keywords: Microcirculation; Flow Resistance; Porous Media; Outflow Boundary Conditions; Haemodynamics

1 Introduction

The microcirculation can be defined as a network of microvessels connecting the large arterial sys-tem to the perfused tissues. Due to its morphology and function, such downstream vasculature constitutes the site of major blood pressure drop along the cardiovascular system [1]. Heterogeneous rheological, and cellular-regulated features [15, 9] make the blood-wall dynamics of this system ex-tremely complex, hindering the comprehensive modelling representation. Recently, several detailed computational models were introduced for studying microvascular blood perfusion in various types of tissue but rarely these are coupled with the systemic circulation [13, 23, 12, 19].

Computational haemodynamics has established itself as an efficient and reliable tool for inferring key information on the current cardiovascular flow state of a patient or predicting potential outcomes for various pathophysiological scenarios [2, 28, 7, 22, 8, 10, 6, 4, 5, 18]. These models are generally used for studying the detailed fluid dynamics occurring within large arteries, whereas microcirculation is generally represented via a simplified lumped model, calibrated in order to reflect patient peripheral flow measurements [17]. Driven by the necessity to have a less-user dependent representation of the downstream resistance, the authors introduced a model [11] in which the microvascular flow is treated via a porous media based approach. This study suggested that accurate predictions may be made by employing a lower number of microvascular parameters. However, the challenge remains in estimating the accuracy of porous media models for vascular resistance. The complete experimental validation of a blood network model may be a cumbersome task due to the limited number of *in vivo* available data, and the challenges associated with vascular resistance measurements. From a clinical point of view, the quantitative assessment of microvascular function is carried out by means of various techniques including magnetic resonance, near-infrared spectroscopy and Doppler ultrasound, but these generally provide information only about one specific body region, limiting their representativity at systemic level [20]. On the other hand, various *in vitro* models reproducing arterial flow in tube networks have been developed in order to either extract key system properties or assess the accuracy of their numerical counterparts [24, 25, 14, 21]. Segers and co-workers [24, 25] proposed an *in vitro* network constituted by 37 tapering tubes, in which the peripheral branches are represented by a system consisting of an adaptable pierced rubber cylinder mounted in a syringe, and an adjustable air chamber connected in parallel. Matthys et al. [14] defined an experimental 1:1 replica of the human arterial tree, consisting of 37 silicone branches representing the large conduit vessels. In this case, the downstream passive resistance was represented by single flexible plastic tube, placed before an overflow reservoir.

Recently, porous media models have gained an enormous popularity within the biomechanics community, since they can be used for representing various complex multi-physics problems. Examples range from modelling transport phenomena through the arterial wall, to numerical studies on microwave ablation and drug delivery [29, 30, 31, 32].

In the present work, we analyse the fluid dynamics through a porous media by employing a combined experimental and theoretical approach. The scope of this study is twofold: i) further *in vitro* validation of the theoretical model presented in [11], and ii) characterization of the developed experimental model for reproducing realistic microvascular blood flow conditions. It is important to remark that, despite the characteristic non-Newtonian nature of blood flow, in the current study a Newtonian type fluid is adopted in both experimental and numerical simulations. This simplification is justified by the fact that here the focus is on the underlying link between porous media configuration and the corresponding microvascular resistive effect on blood waveforms. Furthermore, considering a non-Newtonian fluid would surely enhance further the model fidelity with respect to the arterial microvascular case, but at the same time it would lead to a cumbersome model complexity. In the following section, details about the experimental set-up are reported, followed by a description of the key components of the computational framework. In the Section 3, results for different porous media cases are reported, and the effect of tube compliance as well as fluid viscosity on the numerical results is investigated. In the final section, the major findings are summarized and discussed.

2 Materials and Methods

2.1 Experimental setup

The hydraulic circuit, shown in Figure 1, consists of a pulsatile pump feeding water to a silicon pipe network containing a porous resistance medium. The fluid is taken from and discharged to a reservoir. The length of the porous system, indicated with L_p, is varied to capture the length effect on resistance. The pulsatile pump (TRANDOMED Pulsatile Pump P-120) was employed in order to generate a signal resembling the main features of the physiological flow in mammalian blood circulation. Flow rate was recorded at location (b) in the circuit by means of a flowmeter. Pressure was simultaneously measured at a proximal and distal position with respect to the porous medium (circuit locations (a) and (e), respectively). This was done by means of two micro-tip catheter pressure transducers (Millar Instruments, Houston, TX, USA) for which a two-point calibration technique was applied. The wire catheters were inserted into a Y connector and a bridge amplifier was used for the amplification of the pressure signals. The data acquisition system "LabChart" was used for visualizing the recorded data. The uncertainty associated to the instruments employed in the measurement of flow and pressure are: flow meter $\pm 3\%$ and pressure catheter $\pm 1\%$. Repeatability of measurements was ascertained from multiple experimental trials. The density (ρ) and viscosity (μ) of the fluid employed are assumed to be 1.00 g/cm^3 and 0.0089 poise, respectively. The structural characterization of the silicon tubes requires the definition of material properties such as Young's modulus (E) and Poisson's ratio (ν), and the geometry, in terms of inner radius (r_0) and thickness (h_w). The estimated properties of the silicon tubes are E= 1.026 MPa, ν=0.47, r_0=0.3 cm and h_w=0.2 cm.

2.1.1 Porous media system

The porous system is realized by packing plastic mini-spheres inside a silicon tube. Particles with different diameters (D_p) were employed in order to have: i) a homogenous porous medium case and ii) a heterogeneous counterpart. Whilst in the first case only one type of particles were employed, the latter presents three equal-size layers of particles with diameter decreasing along the direction of the flow. Particle migration was prevented by installing a fine-mesh cloth filter (thickness $\approx$ 1 mm, pore diameter $\approx$ 0.5 mm) at the terminal section of the porous system. The porosity (ϵ) of

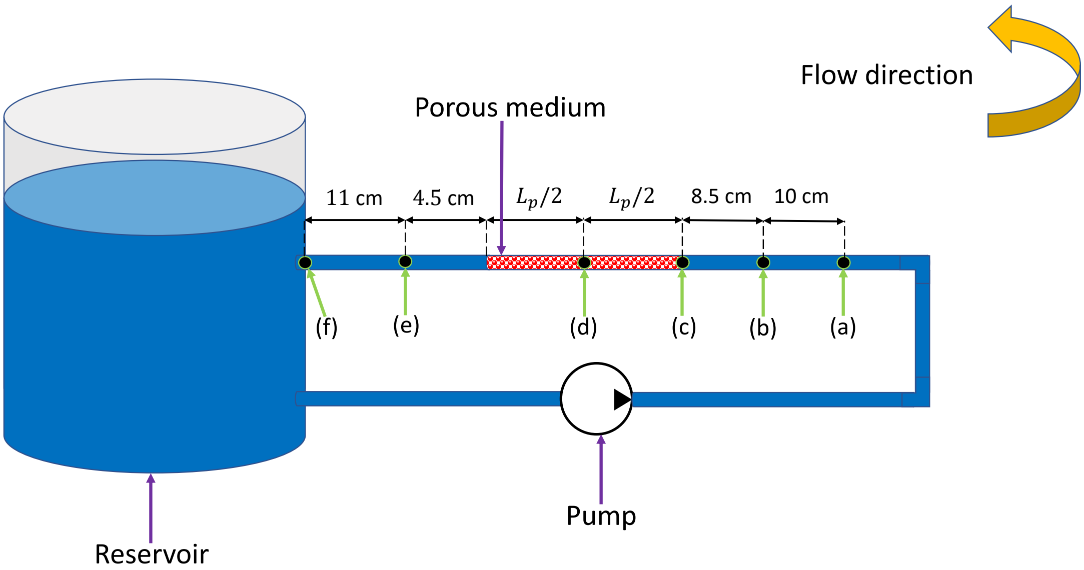

Figure 1: Schematic of the experimental set-up where L_p indicates the length of the porous medium.

the each porous layer was calculated as the ratio of averaged void area between mini-spheres (on the plane perpendicular to flow) over the tube sectional area. In the homogeneous porous resistance, the porosity remains unaltered along the flow direction, as well as for the particle diameter. The length of this porous system (L_p) is 13 cm, the particle diameter (D_p) is 0.148 cm and the porosity (ϵ) is 0.648.

The heterogeneous medium presents three equal-size layers ($L_p/3$=5 cm each) having porosity that decreases in a piecewise manner (ϵ=0.786, 0.684, 0.533) along the flow direction according to the particle size (D_p=0.151, 0.148, 0.131 cm). The space configuration of these porous media as well as the porosity distribution are detailed in the upper left panels of Figure 2 and Figure 4.

2.2 Computational model

A complete description of the computational model adopted is reported in [11]. Here we report the governing equations and boundary conditions of the problem. Flow in 1D poro-elastic tubes (along x direction) is assumed to be laminar, incompressible, Newtonian and is expressed in terms of cross-sectional area (A) and averaged velocity (u) over the cross-section. These are related via

$$\begin{aligned} \frac{\partial(\epsilon A)}{\partial t} + \frac{\partial(\epsilon A u)}{\partial x} = 0, \\ \frac{\partial u}{\partial t} + u\frac{\partial u}{\partial x} + \frac{\beta}{2\rho\sqrt{\epsilon A}}\frac{\partial(\epsilon A)}{\partial x} + \frac{\mu u}{\rho}(\frac{8\pi}{\epsilon A} + \frac{1}{k_p}) = 0, \end{aligned} \tag{1}$$

where t is time, ϵ is the medium porosity (x dependent), whilst k_p is the permeability of the medium, which is assumed to be dependent on porosity:

$$k_p = \frac{\epsilon^3 D_p^2}{150(1-\epsilon)^2}. \tag{2}$$

The porosity field ϵ along the space coordinate x is prescribed in a stepwise fashion according to the values reported in Section 2.1. It is worth mentioning that the product ϵA is referred throughout the manuscript as 'effective area'. Luminal fluid pressure (P) is related to the cross-sectional area as follows

$$P = P_{ext} + \beta(\sqrt{\epsilon A} - \sqrt{\epsilon A_0}), \tag{3}$$

where P_{ext} is the transmural pressure, A_0 is the unstressed cross-section area A_0=πr_0^2, and β is a parameter representing the wall elasticity. The latter parameter can be expressed as

$$\beta = \frac{\sqrt{\pi} h_w E}{A_0(1-\nu^2)}. \tag{4}$$

Boundary conditions at the inlet and exit are required for each primitive variable. The prescription of inlet and outlet variables is carried out by means of forward and backward characteristic variables (w_1 and w_2, respectively) as

$$\begin{aligned} w_1 &= u + 4\sqrt{\frac{\beta\sqrt{\epsilon A}}{2\rho}}, \\ w_2 &= u - 4\sqrt{\frac{\beta\sqrt{\epsilon A}}{2\rho}}. \end{aligned} \tag{5}$$

It is worth noting that these variables may be also used for transmitting information across network discontinuities. At the inlet total pressure (P_{in}) is prescribed. This allows to evaluate

$$\begin{aligned} A_{in}^{n+1} &= \frac{1}{\epsilon}\Big(\frac{P_{in}^{n+1} - P_{ext}}{\beta} + \sqrt{\epsilon A_0}\Big)^2, \\ u_{in}^{n+1} &= w_2^{n+1} + 4(A_{in}^{n+1})^{1/4}\sqrt{\frac{\beta}{2\rho}}, \end{aligned} \tag{6}$$

in which w_2 is calculated via linear extrapolation in the $x-t$ plane. The inlet of the computer model corresponds to point (a) in the circuit (see Figure 1), where the pressure before the porous media is measured. In the experiment, the fluid is discharged from the circuit into the reservoir. In the computational model, the outlet is defined as the last node of the tube before the reservoir, indicated with point (f) in Figure 1. The presence of the reservoir requires accounting for non-negligible wave reflections, and hence, this cannot be modelled as pure absorbing outflow condition. Calculation of the backward characteristic variable at the system's outlet is carried out by imposing a reflection coefficient (R_t) on the last node of the terminal vessel

$$w_2^{n+1} = w_2^0 - R_t(w_1^{n+1} - w_1^0), \tag{7}$$

where w_1 is extrapolated, whilst w_1^0 and w_2^0 are the initial values of w_1 and w_2, respectively. Once w_1 and w_2 at the outlet node are known, the corresponding primitive variables can be obtained by re-arranging (5). For more details about the boundary condition prescription via characteristic variables, see the reference work [16]. System (1) is numerically solved by employing the Locally Conservative Galerkin (LCG) finite element method [26, 27, 16]. The time step and element size are kept constant throughout all simulations, equal to $5 \cdot 10^{-2}$ cm and $2.5 \cdot 10^{-6}$ s, respectively.

3 Results and discussion

3.1 Constant porosity medium

Here, the performances of the resistor with constant porosity profile are assessed. Two constant porosity profiles in space are considered (see the upper left panel of Figure 2) in order to evaluate the effect of the jump in effective area occurring at the interface (c). The profile ϵ_1, the real value, indicates a sharp variation in porosity after point (c), whilst ϵ_2 corresponds to a more gradual change of porosity in space. The pressure experimentally recorded at point (a) is depicted in the upper right panel of Figure 2 and is used as input in the numerical model.

The lower panels of Figure 2 show the computed pressure at point (e) and flow at point (b) respectively, along the corresponding measurements obtained from the *in vitro* experiment. The numerical results are reported for different reservoir reflection coefficients and porosity profiles. The discrepancy between measurements and numerical predictions is quantified by means of the corresponding time-dependent and mean value relative errors (see Table 1), indicated respectively with χ_P, χ_Q and $\chi_{\bar{P}}$, $\chi_{\bar{Q}}$. These errors are calculated by following [3] (see Appendix A1).

It is clear that reflections generated in the reservoir play an important role in this system's fluid dynamics. If both pressure and flow results are considered, a reflection coefficient between 0.3 and 0.4 seems to provide the best approximation of the experimental data. In order to investigate the role of the reflection coefficient on the pressure waveform, a decomposition of the pressure signal recorded at point (e) into forward and backward components was carried out (see Appendix A2). This analysis clearly shows that the augmentation in pressure occurred for higher R_t is due to an increasing backward pressure, whilst the forward pressure remains almost unaltered. It is worth stating that,

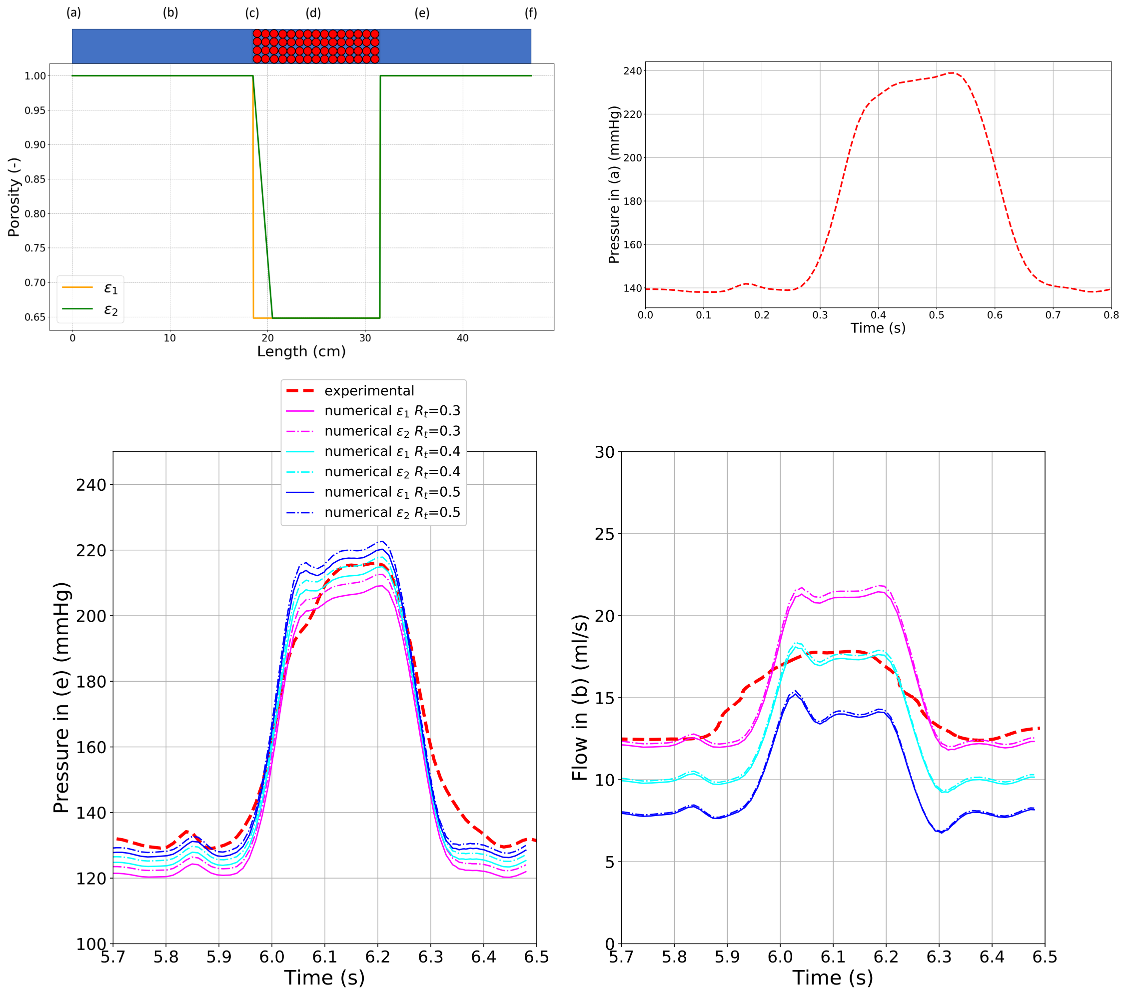

Figure 2: Constant porosity medium: porosity field along the system length (upper left panel); experimental pressure recorded at point (a) in time (upper right panel); comparison between experimental and simulated pressure at point (e) in time (lower left panel); comparison between experimental and simulated flow rate at point (b) in time (lower right panel).

in the theoretical model, this coefficient is fixed and does not depend on the flow conditions at the outflow node, which are variable in time. A flow-dependent coefficient might further diminish the difference between numerical and *in vitro* data. However, the identification of a suitable function representing this effect in time is beyond the scope of this work. On the other hand, the ϵ profile choice seems to have a moderate but distinguishable effect on the results, especially for the pressure recorded after the porous media. Between the two profiles, the gradual porosity variation (ϵ_2) seems to be slightly better represent what is observed experimentally.

	χ_P (%)	χ_Q (%)	$\chi_{\bar{P}}$ (%)	$\chi_{\bar{Q}}$ (%)
ϵ_1 R_t=0.3	6.3	7.4	5.8	3.2
ϵ_2 R_t=0.3	4.9	7.5	4.3	5.0
ϵ_1 R_t=0.4	4.2	12.6	3.3	15.6
ϵ_2 R_t=0.4	3.5	11.9	2.0	14.4
ϵ_1 R_t=0.5	3.1	26.2	0.9	32.8
ϵ_2 R_t=0.5	2.7	25.6	0.1	32.1

Table 1: Relative errors of the simulated pressure in (e) and flow rate in (b) for the homogenous porous media case (sampling rate equal to 2 kHz). $\bar{P}$ and $\bar{Q}$ refer to mean values of P and Q.

Figure 3 provides a snapshot of what happens at different locations of the system, for different outflow reflective conditions. Velocity is substantially increased when the fluid passes through the

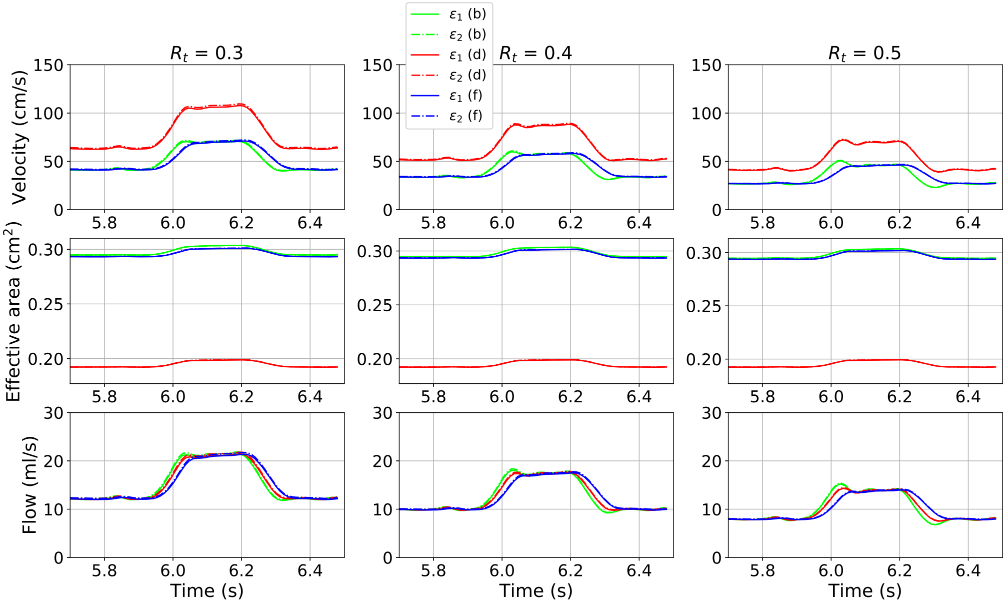

Figure 3: Velocity, effective area and flow rate recorded in time at network locations (b), (d) and (f) for the case with a constant porosity medium.

porous media. This can be attributed to the significantly reduced effective area characterizing the porous media, in conjunction with the conservation of volumetric flow. Interestingly, whilst the average value of velocity decreases by increasing the reflection coefficient, the effective area profile remains essentially insensitive to this outflow condition. Accordingly to this, the flow reduction is observed for higher values of R_t. Furthermore, both velocity and flow exhibit more pronounced high and low peaks at the inlet for the cases with more reflections. Contrary to pressure, velocity and area do not seem to be significantly affected by the gradually changing porosity profile.

3.2 Variable porosity medium

In this section, the porous media with variable properties along the longitudinal length is examined. The porosity profiles shown in the upper left panel of Figure 4 reflect the heterogeneous geometric dimensions reported in Section 2.1.1, with ϵ_2 as gradually changing counterpart to ϵ_1. With respect to the previous case, a similar pressure signal at inlet was recorded (see the upper right panel of Figure 4). The small discrepancy between the two pressures measured at the inlet may be justified by the fact that the reservoir flow reflection is dependent on the pressure after the porous media.

As expected, the heterogeneous porous media offers a greater resistance to flow than the homogeneous counterpart, as shown in the lower panels of Figure 4. Between these two porous media cases, the experimental values of pressure at point (e) are indeed significantly different. In the variably porosity case, the pressure peak reads approximately 200 mmHg whilst with the constant porosity the maximum value reaches almost 220 mmHg. On the other hand, the situation regarding the average lowest pressure is opposite (approximately 130 mmHg and 120 mmHg for the constant and variable porosity, respectively). This comparison may be considered meaningful since the flow waveform through the system is essentially unaltered (see flow signals in the lower right panels of Figure 2 and Figure 4).

For the variable porosity media, identifying the optimal reservoir reflection coefficient characterizing the system fluid dynamics is more complex. For a high value of R_t the computed pressure at point (e) better approximates the measured curve, but the flow is underestimated. The opposite situation occurs if low value of R_t is selected. This is reflected in the relative errors of the simulated pressure and flow reported in Table 2. Therefore, the best trade-off value seems to be around 0.3 again, but in this case the difference between experimental and theoretical results is stark. This probably because the increase in fluid-dynamics complexity associated with the variable step-change porosity can only be partially represented by the 1D model. Furthermore, for this system, gradually changing porosity profile at point (c) does not significantly affect the results. The computed velocity, effective area and flow at locations (b), (d) and (f) present the same pattern as for the case with constant porosity (see Appendix A3).

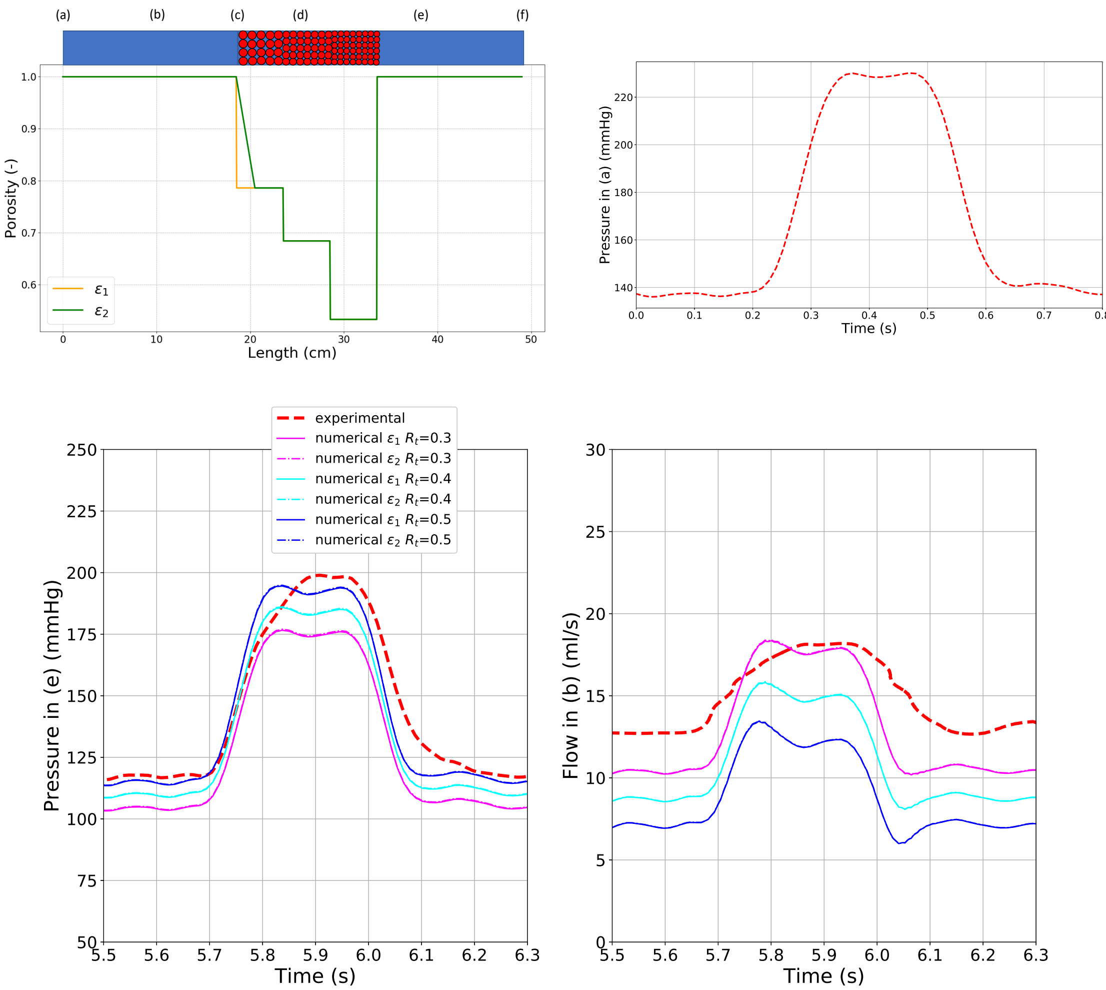

Figure 4: Variable porosity medium: porosity field along the system length (upper left panel); experimental pressure recorded at point (a) in time (upper right panel); comparison between experimental and simulated pressure at point (e) in time (lower left panel); comparison between experimental and simulated flow rate at point (b) in time (lower right panel).

	χ_P (%)	χ_Q (%)	$\chi_{\bar{P}}$ (%)	$\chi_{\bar{Q}}$ (%)
ϵ_1 R_t=0.3	11.2	11.0	11.1	13.2
ϵ_2 R_t=0.3	11.0	10.9	10.8	13.0
ϵ_1 R_t=0.4	6.9	21.7	6.5	27.2
ϵ_2 R_t=0.4	6.7	21.6	6.3	27.1
ϵ_1 R_t=0.5	3.6	32.4	2.2	40.6
ϵ_2 R_t=0.5	3.5	32.3	2.0	40.5

Table 2: Relative errors of the simulated pressure in (e) and flow rate in (b) for the heterogeneous porous media case (sampling rate equal to 2 kHz). $\bar{P}$ and $\bar{Q}$ refer to mean values of P and Q.

3.3 Fluid viscosity and wall elasticity effects

Here, how the fluid viscosity and wall Young's modulus impact the porous media fluid-dynamics is investigated. For the sake of simplicity, only the constant porosity medium with profile ϵ_2 is considered. The viscosity and Young's modulus reported in Section 2.1.1 are taken as reference values and are indicated with μ_{ref} and E_{ref}, respectively. In general, employing a more viscous fluid than the reference one implies increasing the pressure drop across the porous media and limiting the flow, and vice versa if the viscosity is decreased (see Figure 5). Increasing the reflection coefficient reduces the average flow and minimizes the differences in magnitude between different viscosity fluids.

Interestingly, the flow through the system can be substantially modulated by the level of tube

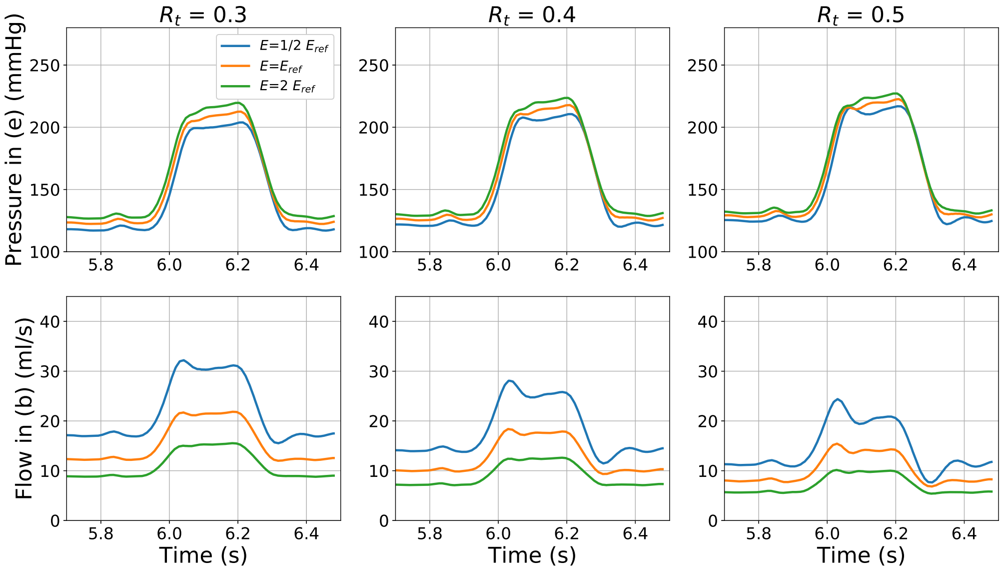

Figure 5: Impact of dynamic viscosity on pressure at point (e) and flow rate at point (b) for different reservoir reflection coefficients.

elasticity, almost without altering the pressure waveform as shown in Figure 6. It is observed that, with larger reflection coefficients, the flow waveform peaks for the very elastic tube appear more pronounced. These results may suggest that the discrepancy between numerical and experimental data reported in the previous sections could be partially due to an inexact estimation of the reference Young's modulus. Also, it is worth to point out that the pressure-area relationship adopted for characterizing the wall structural response might have a non-negligible effect on the results. This is because the silicon, as well as the arterial wall, exhibits a non-linear behaviour under high pressure load, which could be better captured by employing a more complex hyper-elastic solid formulation. It is also important to mention that a previous work investigated the effect of resonances on pulsatile

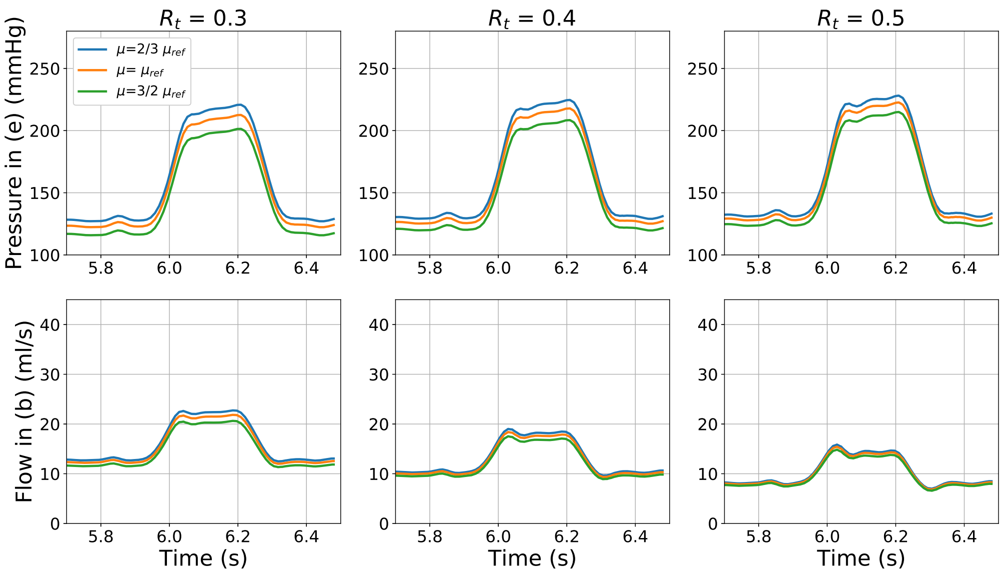

Figure 6: Impact of Young's modulus on the pressure at point (e) and flow rate at point (b) for different reservoir reflection coefficients.

pressure-driven Newtonian flow confined in elastic vessels [34]. This study elucidated the underlying link between resonance frequency and system's parameters (such as fluid viscosity and Young's modulus) and how the variation of the latter may enhance the dynamic permeability. Interestingly, they showed that the resonance frequency cannot exist beyond a certain value of the ratio between the elastic wall frequency and the fluid viscous frequency. According to this analysis, resonance phenomena may not be relevant for the current model's settings. However, this conclusion is limited by the presence of two elements which were not accounted for in [34]: i) the variability of the effective area of the poro-elastic tube along the axial direction, and ii) the non-negligible advective term. We reiterate that further studies are necessary in order to shed the light on these aspects.

4 Conclusion

This work attempted to characterize the microcirculation at macroscopic fluid dynamics level by using a systemic circulation model. A porous media-based model introduced in [11] for representing microvascular flow resistance was employed against data obtained from an *in vitro* experimental set-up. The intrinsic complexity of the experiment associated with backward reflections due to tube compliance and reservoir was dealt with by employing the characteristic variables in the 1D Navier Stokes formulation. The comparison between simulated and *in vitro* data shows that the reflections play a primary role in the system fluid dynamics. On the other hand, the choice regarding how to model the porosity profile at media entry does not seem to significantly affect the results. The flow rate was preserved throughout the network, imposing a significant increase in fluid velocity within the porous medium. The variable porosity media, with respect to homogenous one, reduces the difference between peak systolic and diastolic pressure. Furthermore, the fluid dynamics occurring through the variable porosity medium is not captured by the theoretical model as well as for the simpler porous configuration. This may be due to the presence of turbulence 3D reflections at the interfaces between different particle layers that are not fully represented by a 1D model. Overall, however, a good agreement between *in vitro* results and theoretical model demonstrates that the proposed poro-elastic vessel model is valid apart. It is worth reporting that no parameters tuning was applied during the validation process. This reinforces the idea that the present model is capable of representing realistic conditions with a limited number of inputs. Besides the validation, a concise sensitivity analysis was carried out in order to show which elements could be modified if different microcirculatory conditions need to be considered. As expected, fluid viscosity plays a non-negligible role in attenuating the flow. Also, the pressure at the outlet is reduced if a more viscous fluid is employed. The vessel elasticity can significantly affect the average fluid flow whilst the pressure is essentially unaltered. This finding is crucial if the proposed setting is employed for representing larger (in volume) downstream circulations. It is important to mention that the current findings were obtained by employing a Newtonian fluid, and these cannot be considered fully representative of realistic blood flow conditions. The *in-vitro* network, per se, is only partially able to reflect the complex features of microvascular networks. Future studies are therefore necessary for i) investigating the role of non-Newtonian fluid behaviour on the poro-elastic fluidynamic response, ii) identifying the corresponding model parameters and eventual adaptations for representing more realistic microvascular scenarios. Finally, the proposed framework can also be further improved and extended in order to account for various features and phenomena, including network tortuosity, transport of species within the tissues and mechanical compression.

Aknowledgements

This work was funded by UKRI GCRF collaborative grant RIG1032-111 between Swansea University and IIT Madras.

References

[1] Adjoua, O., Pitre-Champagnat, S., Lucor, D., 2019. Reduced-order modeling of hemodynamics across macroscopic through mesoscopic circulation scales. *International Journal for Numerical Methods in Biomedical Engineering*, 35(12), e3274.

[2] Alastruey, J., Parker, K.H., Peiro, J., Byrd, S.M., Sherwin, S.J., 2007. Modelling the circle of Willis to assess the effects of anatomical variations and occlusions on cerebral flows. *Journal of biomechanics*, 40(8), 1794-1805.

[3] Alastruey, J., Khir, A.W., Matthys, K.S., Segers, P., Sherwin, S.J., Verdonck, P. R., Parker, K.H., Peiró, J., 2011. Pulse wave propagation in a model human arterial network: assessment of 1-D visco-elastic simulations against in vitro measurements. *Journal of biomechanics*, 44(12), 2250-2258.

[4] Carson, J., Lewis, M., Rassi, D., van Loon, R., 2019. A data-driven model to study utero-ovarian blood flow physiology during pregnancy. *Biomechanics and modeling in mechanobiology* 18(4), 1155-1176.

[5] Carson, J.M., Roobottom, C., Alcock, R., Nithiarasu, P., 2019. Computational instantaneous wave-free ratio (IFR) for patient-specific coronary artery stenoses using 1D network models. *International Journal for Numerical Methods in Biomedical Engineering* 35(11), e3255.

[6] Charlton, P.H., Mariscal Harana, J., Vennin, S., Li, Y., Chowienczyk, P., Alastruey, J., 2019. Modeling arterial pulse waves in healthy aging: a database for in silico evaluation of hemodynamics and pulse wave indexes. *American Journal of Physiology-Heart and Circulatory Physiology* 317(5), H1062-H1085.

[7] Coccarelli, A., Boileau, E., Parthimos, D., Nithiarasu, P., 2016. An advanced Computational Bioheat Transfer Model for a Human Body with An Embedded Systemic Circulation. *Biomech Model Mechanobiol* 15(5), 1173-1190.

[8] Coccarelli, A., Boileau, E., Parthimos, D., Nithiarasu, P., 2017. Modelling accidental hypothermia effects on a human body under different pathophysiological conditions. *Med Biol Eng Comput* 55, 2155-2167.

[9] Coccarelli, A., Edwards, D.H., Aggarwal, A., Nithiarasu, P., Parthimos, D., 2018. A multiscale active structural model of the arterial wall accounting for smooth muscle dynamics. *Journal of the Royal Society Interface* 15, 20170732.

[10] Coccarelli, A., Hasan, H. M., Carson, J., Parthimos, D., Nithiarasu, P., 2018. Influence of ageing on human body blood flow and heat transfer: A detailed computational modelling study. *International Journal for Numerical Methods in Biomedical Engineering*, e3120.

[11] Coccarelli, A., Prakash, A., Nithiarasu, P., 2019. A novel porous media-based approach to outflow boundary resistances of 1D arterial blood flow model. *Biomech Model Mechanobiol* 18, 939-951.

[12] El-Bouri, W.K., Payne, S.J., 2018. Investigating the effects of a penetrating vessel occlusion with a multi-scale microvasculature model of the human cerebral cortex. *NeuroImage* 172, 94-106.

[13] Hyde, E.R., Cookson, A.N., Lee, J., et al., 2013. Multi-Scale Parameterisation of a Myocardial Perfusion Model Using Whole-Organ Arterial Networks. *Annals of Biomedical Engineering* 42(4):797-811.

[14] Matthys, K.S., Alastruey, J., Peiró, J., Khir, A.W., Segers, P., Verdonck, P., Parker, K.H., Sherwin, S.J., 2007. Pulse wave propagation in a model human arterial network: Assessment of 1-D numerical simulations against in vitro measurements. *Journal of biomechanics*, 40, 3476-3486.

[15] Murtada, S-I., Humphrey, J.D., 2018. Regional heterogeneity in the regulation of vasoconstriction in arteries and its role in vascular mechanics. In: Fu, B., Wright, N. (Eds.), Molecular, Cellular, and Tissue Engineering of the Vascular System. Springer, pp. 105-128.

[16] Mynard, J.P., Nithiarasu P., 2008. A 1D arterial blood flow model incorporating ventricular pressure, aortic valve and regional coronary flow using the locally conservative Galerkin (LCG) method. *Communications in Numerical Methods in Engineering*, 24, 367-417.

[17] Olufsen, M.S., Peskin, C.S., Kim, W.Y., Pedersen, E.M., Nadim, A., Larsen, J., 2000. Numerical Simulation and Experimental Validation of Blood Flow in Arteries with Structured-Tree Outflow Conditions. *Annals of Biomedical Engineering*, 28, 1281-1299.

[18] Pirola S., Guo B., Menichini C., Saitta S., Fu W., Dong Z., Xu X.Y., 2019. 4D flow MRI-based computational analysis of blood flow in patient-specific aortic dissection. *IEEE Transactions on Biomedical Engineering* 66, 3411-3419.

[19] Possenti, L., Giustina Casagrande, G., Di Gregorio, S., Zunino, P., Costantino, M.L., 2019. Numerical simulations of the microvascular fluid balance with a non-linear model of the lymphatic system. *Microvascular Research* 122, 101-110.

[20] Rosenberry, R., Nelson, M. D., 2019. Reactive hyperemia: a review of methods, mechanisms, and considerations. *American Journal of Physiology-Regulatory, Integrative and Comparative Physiology*, R605-R618.

[21] Rotman, O.M., Zaretsky, U., Shitzer, A., Einav, S., 2017. Pressure drop and arterial compliance-Two arterial parameters in one measurement. *Journal of biomechanics*, 50, 130-137.

[22] Sazonov, I., Khir, A. W., Hacham, W. S., Boileau, E., Carson, J., van Loon, R., Ferguson, C., Nithiarasu, P., 2017. A novel method for non-invasively detecting the severity and location of aortic aneurysms. *Biomechanics and modeling in mechanobiology* 16(4), 1225-1242.

[23] Schmid, F., Tsai, P.S., Kleinfeld, D., Jenny, P., Weber, B., 2017. Depth-dependent flow and pressure characteristics in cortical microvascular networks. *PLos Comput Biol* 13(2), e1005392.

[24] Segers, P., Dubois, F., De Wachter, D., Verdonck, P., 1998. Role and Relevancy of a Cardiovascular Simulator. *Cardiovascular Engineering* 3(1), 48-56.

[25] Segers, P., Verdonck, P., 2000. Role of tapering in aortic wave reflection: hydraulic and mathematical model study. *Journal of Biomechanics* 33, 209-306.

[26] Thomas, C.G., Nithiarasu, P., Bevan, R.L.T., 2008. The locally conservative Galerkin (LCG) method for solving the incompressible Navier-Stokes equations. *International Journal of Numerical Methods in Fluids* 57, 1771-1792.

[27] Thomas, C.G., Nithiarasu, P., 2008. An element-wise, locally conservative Galerkin (LCG) method for solving diffusion and convection-diffusion problems. *International Journal of Numerical Methods in Engineering* 73, 642-664.

[28] Xiao, N., Alastruey, J., Figueroa, C.A., 2014. A systematic comparison between 1-D and 3-D hemodynamics in compliant arterial models. *International Journal for Numerical Methods in Biomedical Engineering* 30(2), 204-231.

[29] Iasiello, M., Vafai, K., Andreozzi, A., Bianco, N., Tavakkoli, F., 2015. Effects of external and internal hyperthermia on LDL transport and accumulation within an arterial wall in the presence of a stenosis. Annals of biomedical engineering, 43(7), 1585-1599.

[30] Rattanadecho, P., Keangin, P, 2013. Numerical study of heat transfer and blood flow in two-layered porous liver tissue during microwave ablation process using single and double slot antenna. International Journal of Heat and Mass Transfer, 58(1-2), 457-470.

[31] Støverud, K. H., Darcis, M., Helmig, R., Hassanizadeh, S. M., 2012. Modeling concentration distribution and deformation during convection-enhanced drug delivery into brain tissue. Transport in porous media, 92(1), 119-143.

[32] Andreozzi, A., Iasiello, M., Netti, P. A., 2019. A thermoporoelastic model for fluid transport in tumour tissues. Journal of the Royal Society Interface, 16(154), 20190030.

[33] Willemet, M., Alastruey, J., 2015. Arterial Pressure and Flow Wave Analysis Using Time-Domain 1-D Hemodynamics. Annals of Biomedical Engineering, 43(1), 190-206.

[34] Aimee M. Torres Rojas, I. Pagonabarraga, and E. Corvera Poiré, 2017. Resonances of Newtonian fluids in elastomeric microtubes. Physics of Fluids 29, 122003.

Appendix

A1: Relative error calculation

To assess the accuracy of the simulated pressure and flow, the following time-dependent relative errors are calculated at the monitoring nodes

$$\chi_P = \frac{1}{N}\sum_{i=1}^{N}\sqrt{\left(\frac{P_i^{exp}-P_i}{P_i^{exp}}\right)^2} \quad \text{and} \quad \chi_Q = \frac{1}{N}\sum_{i=1}^{N}\frac{\sqrt{(Q_i^{exp}-Q_i)^2}}{\max(Q^{exp})}, \tag{8}$$

in which N is the total number of samples in one cardiac cycle, the subscript i indicates the sampling point, the superscript exp indicates experimental data and the operator $\max(\cdot)$ indicates the maximum value of the sample. The mean value relative errors are calculated via

$$\chi_{\bar{P}} = \frac{\sqrt{\left(\mathrm{mean}(P^{exp})-\mathrm{mean}(P)\right)^2}}{\mathrm{mean}(P^{exp})} \quad \text{and} \quad \chi_{\bar{Q}} = \frac{\sqrt{\left(\mathrm{mean}(Q^{exp})-\mathrm{mean}(Q)\right)^2}}{\mathrm{mean}(Q^{exp})}, \tag{9}$$

where $\mathrm{mean}(\cdot)$ indicates the mean value of the sample.

A2: Pressure signal decomposition

Here the pressure signal corresponding to the case reported in Section 3.1 is considered. The pressure signal in time P recorded at point (e) is decomposed in forward and backward components, P_f and P_b respectively, by following the methodology reported in [33]. Figure 7 shows how these components vary in time for R_t=0.3, 0.4 and 0.5 and porosity profiles ϵ_1 and ϵ_2. From this comparison it is clear that increasing the reflection coefficient R_T leads to a significant increment in the backward pressure component, whilst the forward pressure component is slightly attenuated. This means that, for higher R_t, the increment in pressure signal magnitude is caused by the increasing backward pressure component.

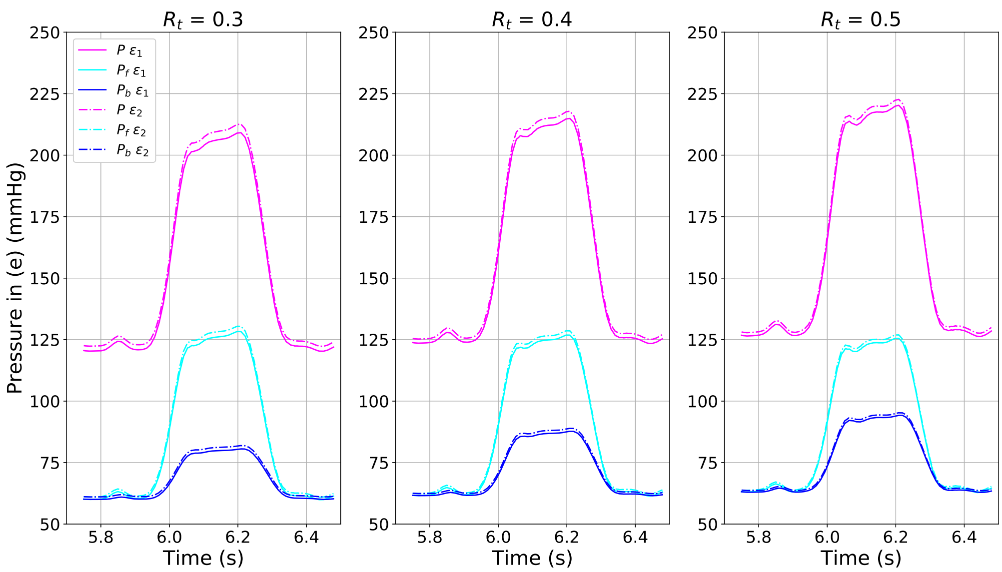

Figure 7: Decomposition of pressure signal recorded at point (e) in forward and backward components.

A3: Flow variables in the variable porosity system

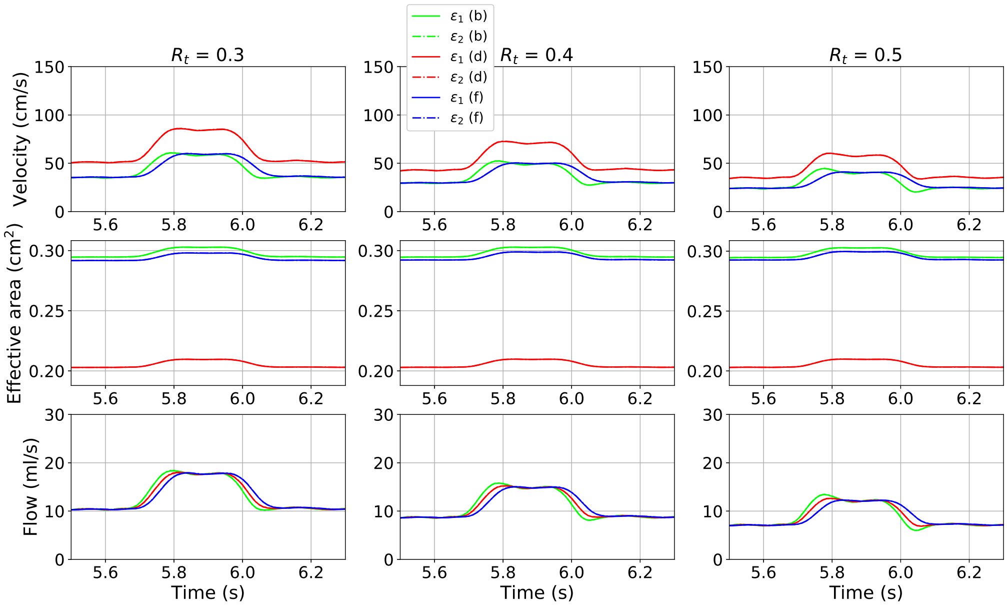

Figure 8: Velocity, effective area and flow rate recorded in time at network locations (b), (d) and (f) for the case with a variable porosity medium.